OIST OKINAWA INSTITUTE OF SCIENCE AND TECHNOLOGY GRADUATE UNIVERSITY
沖縄科学技術大学院大学

Steady viscoelastic flow around high-aspect-ratio, low-blockage-ratio microfluidic cylinders

Author	Simon J. Haward, Kazumi Toda-Peters, Amy Q. Shen
journal or publication title	Journal of Non-Newtonian Fluid Mechanics
volume	254
page range	23-35
year	2018-02-20
Publisher	Elsevier
Rights	(C) 2018 Elsevier B.V.
Author's flag	author
URL	http://id.nii.ac.jp/1394/00000619/

doi: info:doi/10.1016/j.jnnfm.2018.02.009

Creative Commons
Attribution-NonCommercial-NoDerivatives 4.0 International
(https://creativecommons.org/licenses/by-nc-nd/4.0/)

Steady viscoelastic flow around high-aspect-ratio, low-blockage-ratio microfluidic cylinders

Simon J. Haward*, Kazumi Toda-Peters, Amy Q. Shen

Okinawa Institute of Science and Technology Graduate University, 1919-1 Tancha, Onna-son, Okinawa 904-0495, Japan

©2018. *This manuscript version is made available under the CC-BY-NC-ND 4.0 license.* http://creativecommons.org/licenses/by-nc-nd/4.0/

Abstract

We employ a state-of-the-art microfabrication technique (selective laser-induced etching, SLE) to produce microfluidic cylinder geometries that explore new geometrical regimes. Using SLE, two microchannels are fabricated in monolithic fused silica substrate with height $H = 2$ mm and width $W = 0.4$ mm (aspect ratio $\alpha = H/W = 5$) containing cylinders of radius $r = 0.02$ mm (blockage ratio $\beta = 2r/W = 0.1$), centered at the channel mid-width, $W/2$. An 'sc' channel contains a single cylinder, while a 'dc' channel contains two axially-aligned cylinders separated by a distance $L = 1$ mm ($L = 50r$). Compared with cylinder geometries fabricated by soft lithography (which typically have $\alpha \ll 1$ and $\beta \lesssim 0.5$), these rigid glass devices provide a quasi-2D flow along the direction of the cylinder axis and also more clearly reveal the effects of the strong extensional wake regions located at the leading and trailing stagnation points. Using flow velocimetry and quantitative birefringence measurement techniques, we study the behavior of a well-characterized viscoelastic polymer solution in flow around the cylinders. The small cylinder radii result in low inertia and very high elasticity numbers $El \approx 2400$. For the sc device, we report strong flow modification effects around the cylinder as the flow rate is incremented. This is associated with the deformation of polymer molecules primarily in the *upstream* wake region, leading to the onset of a purely elastic flow asymmetry upstream of the cylinder. Stretched polymer molecules are advected around the cylinder and relax downstream of the cylinder, resulting in an extremely long elastic wake extending for $> 300r$ downstream. In the dc channel, at lower flow rates, similar flow modification effects are observed to develop around, and downstream of, both cylinders. However, at higher flow rates the wake of the first cylinder extends $> 50r$ downstream, and begins to interact with the second cylinder. The second cylinder becomes encapsulated by the wake of the first and is effectively obviated from the flow field. The results will be of relevance to understanding practical applications of viscoelastic fluids, for example in particle suspension and porous media flows, and also for benchmarking against numerical simulations using viscoelastic constitutive models.

Keywords: polymer solution, viscoelasticity, microfluidics, cylinder, molecular orientation, flow modification

2010 MSC: 00-01, 99-00

1. Introduction

The creeping flow of viscoelastic fluids around cylinders has long been considered a benchmark system in non-Newtonian fluid dynamics [1]. Being a two-dimensional model for flow around a sphere, flow around a cylinder represents a fundamental example of flow past an obstacle, presenting strong extensional kinematics due to streamwise stagnation points in both the upstream and downstream wake regions, curvature of streamlines and regions of strong shear around the sides of the object. Experimental measurements made under these conditions of mixed kinematics are of great utility for benchmarking vis-

*Corresponding author

Email address: simon.haward@oist.jp (Amy Q. Shen)

coelastic constitutive equations used in numerical simulations [2–5], and are of direct relevance to optimizing a range of practical uses of viscoelastic fluids such as polymer processing applications, flows though porous media, suspension of particles, etc. The extensional kinematics in the up-and downstream wakes of obstacles are a particularly prominent feature of these flows, leading to large microstructural deformation (e.g. elongation of polymer molecules), and resulting in strong flow modification due to the localized enhancement of the stress [6–11]. The experimental study of viscoelastic flows around macroscopic cylinders has a long history [5, 6, 12–17], and in recent years, this study has been extended into the realm of microfluidics [11, 18–27]. Due to the extremely small characteristic length scales involved (cylinder radii, $r \sim O(100\ \mu\text{m})$), microfluidics provide a window into an interesting regime in which inertia is negligible (Reynolds numbers $Re \ll 1$) but elasticity is high (Weissenberg numbers $Wi > 1$). Microscopic viscoelastic flows past cylinders may lend insight into processes such as biological motions of cilia and flagella [28], impregnation of fibrous media by viscoelastic matrix fluids (i.e. formation of composite materials) and coating of e.g. optical fibers with polymeric cladding.

To date, most microfluidic studies of flow around cylinders have focussed on the generation of elastic flow instabilities, i.e. the generation of instability due to elastic forces in the absence of significant inertia. Elastic instabilities typically arise when there is a combination of streamline curvature coupled with high elastic stresses [29–34] and are particularly prevalent in microfluidics due to the high elasticity numbers ($El = Wi/Re$). Geometrically, a cylinder confined inside a rectangular microchannel can be characterized by two ratios of lengthscales: (1) the aspect ratio of the channel $\alpha = H/W$ (where H and W are the channel height and width, respectively), and (2) the degree to which the cylinder blocks the channel, i.e. the *blockage ratio* $\beta = 2r/W$ (where r is the cylinder radius). The aspect ratio of the cylinder itself can also be considered, and this is given by $AR = H/2r = \alpha/\beta$. Due to limitations conferred by the soft polydimethylsiloxane (PDMS) materials normally

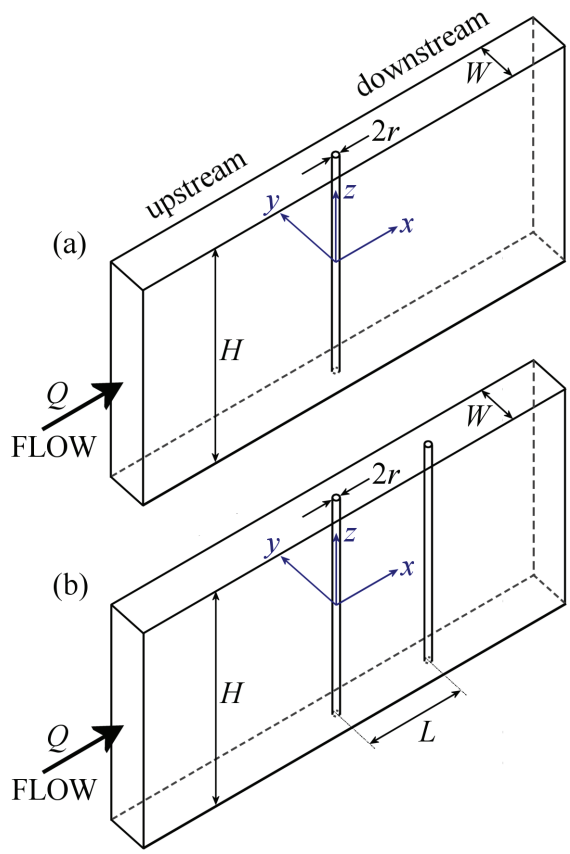

Figure 1: Schematic drawings of (a) the single cylinder (sc) and (b) the double cylinder (dc) devices. Both devices have channel width $W = 0.4$ mm and height $H = 2$ mm (aspect ratio $\alpha = H/W = 5$). All cylinders have a radius $r = 20 \pm 2\ \mu$m. The cylinders themselves have an aspect ratio $AR = H/2r = 50$ and provide a blockage ratio $\beta = W/2r = 0.1$. The centre-centre spacing between cylinders in the dc device is $L = 1$ mm ($= 50r$). The origin of the indicated Cartesian coordinate system is defined as the centre-point of the most upstream cylinder.

used to fabricate microfluidic cylinder devices, their geometries are restricted to rather low aspect ratios ($\alpha < 1$) and also high blockage ratios (typically $\beta \geq 0.5$) [11, 18, 21, 23, 25]. The low aspect ratio means the flow field is inhomogeneous through the channel height, so the problem becomes three-dimensional, while the high blockage ratio results in the formation of narrow gaps between the sides of the cylinder and the channel walls. In this case, viscoelastic fluids respond most strongly to the squeezing flow through the gaps, resulting in the generation of elastic instabilities and recirculations upstream of the cylinder [18, 21, 23], which are highly reminiscent of the insta-

bilities seen with flows into simple plane or hyperbolic contractions [35–37]. Other important aspects of the flow around the cylinder, such as the up- and downstream wake regions, feature much less prominently. It is recognized that to clearly observe the extensional flow in the cylinder wake regions, the blockage ratio should be much lower than $\beta = 0.5$ [12]. This can be achieved in PDMS microfluidics simply by increasing the channel width W [11, 25], however this further compounds the problem of the low aspect ratio.

In this work, we employ the technique of selective laser-induced etching (SLE) [38] to fabricate glass microfluidic cylinder devices in a new geometrical regime featuring both a high aspect ratio and a low blockage ratio, see schematic drawings in Figure 1. We study the flow of a well-characterized dilute viscoelastic polymer solution, and its viscous Newtonian solvent, around a single cylinder radius $r = 20\,\mu$m (Figure 1a), and also around two identical cylinders aligned on the flow axis and separated by a significant distance $L = 50r$ (Figure 1b). The small radius means the Reynolds number remains low ($Re \lesssim 0.023$) and the creeping flow occurs at high elasticity number ($El \approx 2400$). The flow field is characterized in significant detail using micro-particle image velocimetry (μ-PIV) and we also perform flow birefringence measurements to provide complementary information about the regions of high polymer stretching and elongational stress. For viscoelastic creeping flow around the single cylinder, as we increment the Weissenberg number, we observe the growth of elastic stresses in a wide region around the cylinder, accompanied by a significant modification of the flow field compared with the Newtonian case. While the flow remains essentially steady and time-independent, we observe the development of a strong flow asymmetry upstream of the cylinder and a strikingly long downstream wake, which can extend for more than 300 cylinder radii. The results for flow around two aligned cylinders provide insights into the nature of interactions that can occur between objects moving in viscoelastic fluids (e.g. settling particles or swimming organisms) and will be of relevance to understanding flows past sequences of objects, such as around clusters of cilia, in porous media, etc.

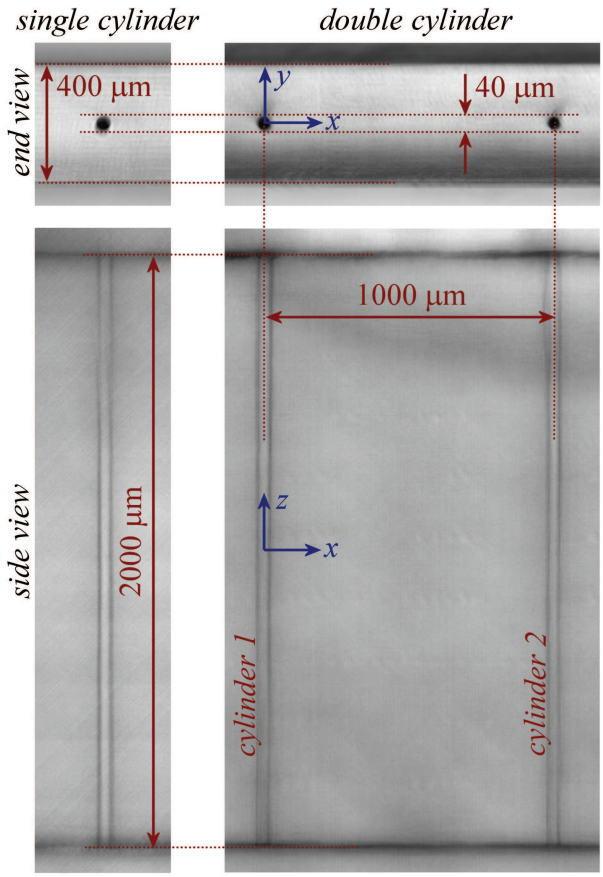

Figure 2: Transmitted light micrographs of the sc and dc microfluidic cylinder devices captured from both end-on and side-on orientations.

The results from both geometries should be of value for benchmarking numerical simulations using viscoelastic constitutive models.

2. Materials and Methods

2.1. Microfluidic device fabrications

The microfluidic cylinder devices depicted schematically in Figure 1 and photographically in Figure 2 were fabricated by SLE in fused silica glass using the state-of-the-art "LightFab" 3D printer (LightFab GmbH, Germany) [39]. The SLE fabrication technique is highly precise, with surface roughness and imperfections of around $\pm 1\,\mu$m. The two channels, one containing a single cylinder (sc) and the other containing two cylinders (dc), both have dimensions of $W = 400\,\mu$m and $H = 2$ mm. This provides a reasonably high aspect ratio $\alpha = 5$, and hence

a good approximation to a two dimensional flow, as will be confirmed in later experiments. The cylinders all have a radius $r = 20\ \mu$m, which results in a low blockage ratio $\beta = 0.1$ and a cylinder aspect ratio $AR = 50$. The centre-centre separation between cylinders in the dc geometry is $L = 1$ mm (or $L = 50r$). Unlike PDMS microfluidics, the single-piece rigid glass construction of each device means the cylinders can be made so long and slender without deforming under an imposed flow. Indeed, in the experiments to be described in the following sections, no measurable deflection of the cylinders was registered. Additional advantageous features of the SLE fabrication method are: amenablity to organic solvents, and optical access to both the *xy* and *xz* planes (see Figures 1 and 2).

2.2. Test fluids

The viscoelastic test solution is composed of a high molecular weight ($M_p = 6.9$ MDa), low polydispersity ($M_w/M_n = 1.09$) sample of atactic polystyrene (a-PS, Agilent Technologies) dissolved in the viscous organic solvent dioctyl phthalate (DOP, Sigma Aldrich) at a concentration of $c = 0.07$ wt%. The overlap concentration for this polymer-solvent system is $c^* \approx 0.5$ wt% [34, 40], so the fluid is considered dilute. The viscosity of the polymeric solution (and the DOP solvent) have been measured in steady shear using an Anton-Paar MCR 502 stress-controlled rheometer fitted with 50 mm diameter 1° cone-and-plate geometry, and the results have been presented in a prior publication [34]. The viscosity of the solvent is $\eta_s = 59$ mPa s and the zero shear viscosity of the polymer solution is $\eta_0 = 71$ mPa s. The polymer solution is essentially non-shear-thinning over 3 decades in shear rate. The relaxation time of the polymer solution is $\lambda = 13$ ms, which was determined by flow birefringence measurements made in an idealized elongational flow device, the optimized shape cross-slot extensional rheometer (or OSCER) [34, 41]. This value for the relaxation time compares well with that estimated using the formula provided by Zimm [42], which yields $\lambda_{Zimm} \approx 14$ ms [43].

2.3. Flow control and dimensionless numbers

Flow through the sc and dc cylinder devices is driven using two high precision neMESYS syringe pumps (Cetoni, GmbH) with 29:1 gear ratios and operating at no less than twice the minimum specified 'pulsation free' dosing rate. The pumps are fitted with 10 mL Hamilton Gastight syringes with one pump infusing fluid into the device at controlled volume flow rate Q, while the other pump withdraws fluid at an equal and opposite rate from the downstream outlet. Connections between the syringes and the microfluidic devices are made using chemically-resistant viton tubing and stainless steel tubing connectors.

We define two different Reynolds numbers to describe the relative strength of inertial to viscous forces in the microfluidic cylinder devices. The Reynolds number for flow in the rectangular channel is:

$$Re_{ch} = \frac{\rho U D_h}{\eta}, \tag{1}$$

where $U = Q/HW$ is the average flow velocity, $D_h = 2WD/(W+D)$ is the hydraulic diameter of the channel. The density of the fluid $\rho = 981$ kg m^{-3} is taken to be the same for both the solvent and the polymer solution, and η is the fluid viscosity.

We also define a Reynolds number for flow around the cylinders:

$$Re = \frac{\rho U r}{\eta}. \tag{2}$$

We use a characteristic Weissenberg number to describe the relative strength of elastic to viscous forces for polymeric flow around the cylinders, which is defined:

$$Wi = \frac{\lambda U}{r}, \tag{3}$$

where U/r is a characteristic deformation rate for the flow.

The elasticity number describes the relative strength of elastic to inertial forces in the polymeric flow:

$$El = \frac{Wi}{Re} = \frac{\lambda \eta}{\rho r^2}. \tag{4}$$

For the non-shear-thinning polymer solution employed here, the elasticity number does not depend on the flow rate and is

a function of the fluid properties and the geometry only, with a value $El \approx 2400$ that indicates inertial effects can be mostly neglected.

2.3.1. Microparticle Image Velocimetry

Flow velocimetry in the cylinder geometries is performed using a volume illumination μ-PIV system (TSI Inc., MN). The test fluid of interest is seeded with 2 μm diameter (concentration $c_p \approx 0.02$ wt%) fluorescent melamine resin tracer particles (MF-FluoOrange-1240, microParticles, GmbH) with excitation/emission wavelength 560/584 nm. The flow geometry is placed on the stage of an inverted microscope (Nikon Eclipse T*i*) and the plane of interest (either $z = 0$ or $y = 0$ plane) is brought into focus. For most of the experiments, to obtain the largest possible field of view, a 4×, NA= 0.13 numerical aperture Nikon PlanFluor objective lens is used. With this combination of microparticles and objective lens, the measurement width over which microparticles contribute to the determination of the velocity field is $\delta_m \approx 160$ μm [44]. In some of the experiments, to obtain higher spatial resolution and lower measurement width, higher magnification, higher numerical aperture objectives are used. The fluid is illuminated through the objective using a dual-pulsed Nd:YLF laser with a wavelength of 527 nm and a time seperation between pulses Δt. Pairs of images of the fluorescing particles are captured in synchronicity with the pairs of laser pulses using a high speed 1280×800 pixel CMOS imaging sensor (Phantom MIRO) operating in frame-straddling mode. At each flow rate examined, the time Δt is set so that the average displacement of particles between the two images in each pair is around 4 pixels. Since the flows examined are steady, 50 image pairs are captured and processed using an ensemble average PIV algorithm (TSI Insight 4G). A recursive Nyquist criterion is employed with a final interrogation area of 16×16 pixels to enhance the spatial resolution and obtain velocity vectors spaced on a square grid of 16×16 μm (with the 4× objective). Further image analysis, generation of contour plots and streamline traces is performed using the software Tecplot Focus (Tecplot Inc., WA).

2.3.2. Flow-Induced Birefringence

Measurements of flow-induced birefringence (FIB) in the microfluidic cylinder geometries are made using a state-of-the-art Exicor MicroImager^{TM} (Hinds Instruments Inc., OR). The system uses a combination of two photoelastic modulators and a stroboscopic monochromatic light source to determine the relevant Mueller matrix components and provide fully quantitative, spatially resolved measurements of the sample retardance δ (in nm), and the angle of the slow optical axis θ [45, 46]. The instrument is equipped with a 2048×2048 pixel 12-bit CCD imaging sensor and various objective lenses. A 2× objective provides the largest field of view of 5×5 mm and hence a spatial resolution of approximately 2.5 μm/pixel. A 5× objective is used in some experiments and provides a field of view of 2×2 mm and hence a spatial resolution of approximately 1 μm/pixel.

The birefringence Δn is related to the retardance δ by the optical pathlength through the material, and can hence be approximated by:

$$\Delta n = \frac{\delta}{H}, \tag{5}$$

which assumes that the flow is completely uniform through the channel height, i.e. that the flow is two-dimensional (2D).

Birefringence arises in flowing polymer solutions due to the optical anisotropy caused by the orientation of polymer chain segments. This occurs as the equilibrium Gaussian coils become strained in velocity gradients in the flow field. Straining can be particularly high in elongational regions of the flow field where streamwise velocity gradients arise, such as near streamwise stagnation points [9, 47–49]. In many polymeric systems, for a range of deformations, it is found that the birefringence is directly related to the principal stress difference ($\Delta\sigma = \sigma_{xx} - \sigma_{yy}$) in the fluid via the stress-optical rule [34, 49–54]:

$$\Delta n = C\Delta\sigma, \tag{6}$$

where the constant of proportionality C is called the stress-

optical coefficient. For polystyrene solutions, the stress-optical coefficient has a value of $C \approx -5 \times 10^{-9}$ Pa^{-1}, which has been shown to hold valid even in strong elongational flows and up to high extensional rates [49, 53–55]. Clearly, to some approximation, the spatially-resolved measurements of δ obtained from the Exicor MicroImager^{TM} can be considered directly proportional to the elastic tensile stress fields in the flowing polymer solution.

3. Results and discussion

3.1. Newtonian flow characterization

Before proceeding to examine viscoelastic flow in the microfluidic cylinder geometries, we first attempt to confirm our expectations of the flow field within the two devices using the pure Newtonian solvent, DOP. This will confirm the accuracy both of our channels and of our measurement methods, and provide a benchmark for comparison against the subsequent measurements made with the non-Newtonian polymer solution.

In Fig. 3 we present flow field measurements made for the Newtonian solvent in the sc channel some distance upstream of the cylinder. Fig. 3(a) shows a contour plot of the normalized x-component of the velocity (u/U), as visualized in the $z = 0$ plane of the device at a channel Reynolds number $Re_{ch} = 0.024$. Fig. 3(b) shows profiles of u/U (averaged over x) for various Re_{ch} taken across the channel width, demonstrating the expected parabolic form. The experimental data agrees well with an infinite series analytical solution for fully-developed Poiseuille flow in a rectangular channel of $AR = 5$ [56]. In contrast to PDMS microfluidics, our devices can simply be rotated through 90° in order to measure the velocity field in the orthogonal ($y = 0$) plane. In Fig. 3(c), we present an example of such a measurement, again showing contours of u/U for the Newtonian solvent at a channel Reynolds number $Re_{ch} = 0.024$. Profiles of u/U (averaged over x) for various Re_{ch} taken through the channel depth are shown in Fig. 3(d), again in comparison with the analytical prediction. Clearly the flow is quite uniform, with almost constant flow velocity about the channel mid-depth for $-0.5 \lesssim z \lesssim 0.5$ mm. Note that the experimental data in Fig. 3(d) lie slightly below the analytical prediction over most of the range of z, while the data in Fig. 3(b) lie much closer to the predicted curve. This is most likely explained by the measurement depth of the μ-PIV ($\delta_m \approx 160$ μm), which is 40% of the channel width, but only 8% of the channel depth.

Newtonian flow around the microfluidic cylinders is illustrated in Fig. 4. In Figs. 4(a) and 4(b) we show examples of velocity fields with superimposed streamlines for flow at $Re = 0.0007$ around the cylinders in the sc and dc devices, respectively. As expected for Newtonian flow at low Re, a high degree of symmetry in the flow field around the cylinders is demonstrated by these contour plots. We also note that in the dc device, the flow becomes essentially fully developed in the ≈ 1 mm gap between cylinders 1 and 2. In Figs. 4(c) and 4(d) we show normalized velocity profiles of $u(x)/U$ taken along the line $y = 0$ over a range of Re in the sc and dc devices, respectively. The experimental data collapse and also compare well with a 3D finite volume numerical simulation performed using ANSYS Fluent. We would point out that the highest Reynolds number shown for the Newtonian characterization in Fig. 4 ($Re = 0.073$) is approximately 3× larger than the maximum Reynolds numbers reached in the subsequent experiments with the viscoelastic polymer solution.

Lastly, in Fig. 5 we examine the flowtype parameter [57–60] for creeping Newtonian flow around a cylinder. The flowtype parameter is defined:

$$\xi(x, y) = \frac{|\dot{\boldsymbol{\gamma}}| - |\boldsymbol{\Omega}|}{|\dot{\boldsymbol{\gamma}}| + |\boldsymbol{\Omega}|}, \tag{7}$$

where $|\dot{\boldsymbol{\gamma}}| = \sqrt{\frac{1}{2}\mathbf{D} : \mathbf{D}}$ and $|\boldsymbol{\Omega}| = \sqrt{\frac{1}{2}\boldsymbol{\Omega} : \boldsymbol{\Omega}}$ are the magnitudes of the deformation rate tensor $\mathbf{D} = \frac{1}{2}(\nabla\mathbf{v}+\nabla\mathbf{v}^{\mathrm{T}})$ and the vorticity tensor $\boldsymbol{\Omega} = \frac{1}{2}(\nabla\mathbf{v}-\nabla\mathbf{v}^{\mathrm{T}})$, respectively, which can be locally evaluated using the components of the velocity vectors $\mathbf{v}= (u, v, w)$ obtained by μ-PIV [34].

The flowtype parameter varies between −1 and 1, with values of −1 corresponding to purely rotational kinematics, values of 0 corresponding to simple shear and values of +1 corresponding to purely extensional kinematics. Figure 5 shows the

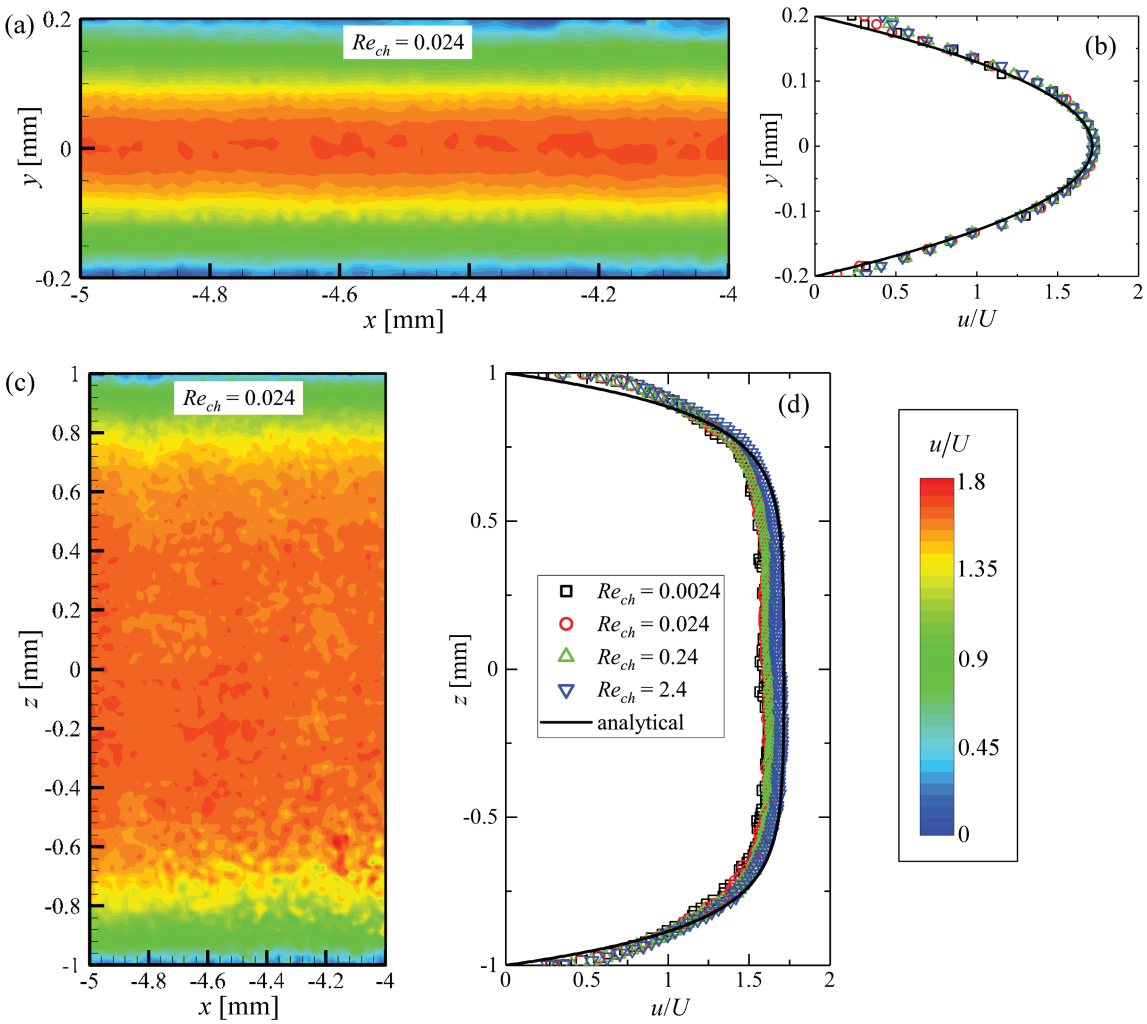

Figure 3: Characterization of the Newtonian flow field in the channel, in a region upstream of the cylinder in the sc device. (a) Contours of the normalized x-velocity component (u/U) in the xy plane at $z = 0$ at a channel Reynolds number $Re_{ch} = 0.024$. (b) Normalized profiles of the streamwise velocity taken across the transverse direction $u(y)/U$ for various channel Reynolds numbers $0.0024 < Re_{ch} < 2.4$, showing a parabolic form. (c) Contours of the normalized x-velocity component (u/U) in the xz plane at $y = 0$ at a channel Reynolds number $Re_{ch} = 0.024$. (d) Normalized profiles of the streamwise velocity taken along the axial direction $u(z)/U$ for various channel Reynolds numbers $0.0024 < Re_{ch} < 2.4$, showing essentially 2D flow within the central region of the channel for $-0.5 < z < 0.5$ mm. The solid lines in parts (b) and (d) show an infinite series analytical solution for creeping Newtonian flow in a channel of $AR = 5$ [56].

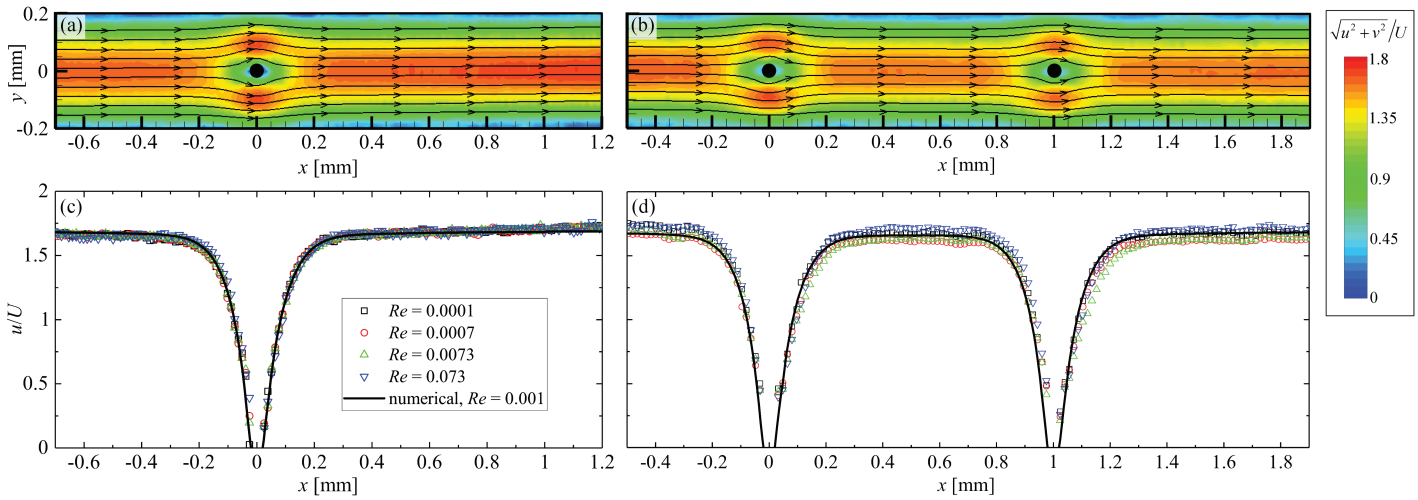

Figure 4: Characterization of the Newtonian flow field around the cylinders in the xy plane at $z = 0$. Contours of the normalized velocity magnitude in (a) the sc device, and (b) the dc device at $Re = 0.0007$. Profiles of the normalized streamwise velocity $u(x)/U$ taken along $y = 0$ over a range of Re in (c) the sc device, and (d) the dc device. The solid lines in parts (c) and (d) are obtained from a three-dimensional finite volume simulation of the flow field performed at $Re = 0.001$.

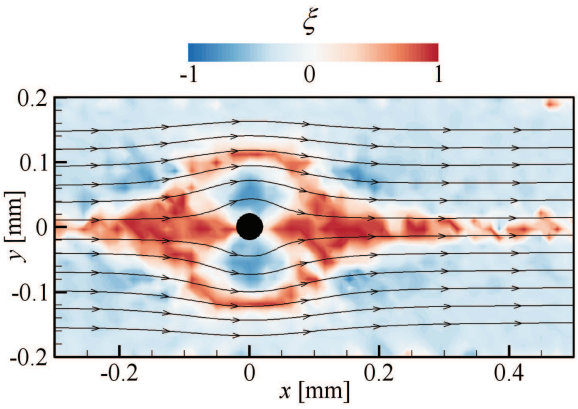

Figure 5: Flowtype parameter around a cylinder at $Re = 0.0007$, determined from μ-PIV measurements made in the sc device.

local flowtype around the cylinder of the sc device computed from the velocity field shown in Fig. 4(a) at a Reynolds number of $Re = 0.0007$. There are regions of strong extensional flow immediately up- and downstream of the cylinder, joined together by a ring of extensionally-dominated kinematics with a radius of $w/2$. The rest of the flow field is largely dominated by shear, with symmetric lobe-like regions of slightly stronger rotation either side of the cylinder. The spatial variation of the flowtype parameter around the cylinder is consistent with recent 2D numerical simulations for Newtonian flow past linear arrays of 'widely spaced' cylinders separated by 6 radii [60].

3.2. *Polymeric flow around a single cylinder*

In this section, we proceed to examine the flow of the dilute polymeric test solution (0.07 wt% of 6.9 MDa a-PS in DOP) around the single microscopic cylinder contained inside the sc flow channel.

The normalized flow velocity magnitude field measured by μ-PIV performed in the $z = 0$ plane of the sc device is shown in Fig. 6(a)-(e) for a range of Weissenberg numbers $1.35 \leq Wi \leq 54.2$ and for low Reynolds number $Re \leq 0.023$. For low Wi (see e.g. Fig. 6(a) for $Wi = 1.35$), the flow field appears Newtonian like (compare with Fig. 4(a)). However, as Wi is progressively increased through Figs. 6(b)-(e), an increasing degree of fore-aft asymmetry develops, with an extended wake developing downstream of the cylinder. Such extended downstream wakes have been reported for polymeric flows around cylinders and spheres before and are attributed to the effects of polymer deformation in the high velocity gradients that are achieved at the downstream stagnation point [2, 7–9, 25]. However, the downstream wakes observed here are particularly dramatic by any standards; in Figs. 6(d) and (e) a fully-developed parabolic flow profile across the channel has still not been acheived even at a distance of 1.9 mm ($95r$) downstream of the cylinder. Additional features to note from Figs. 6(a)-(e) as Wi is increased

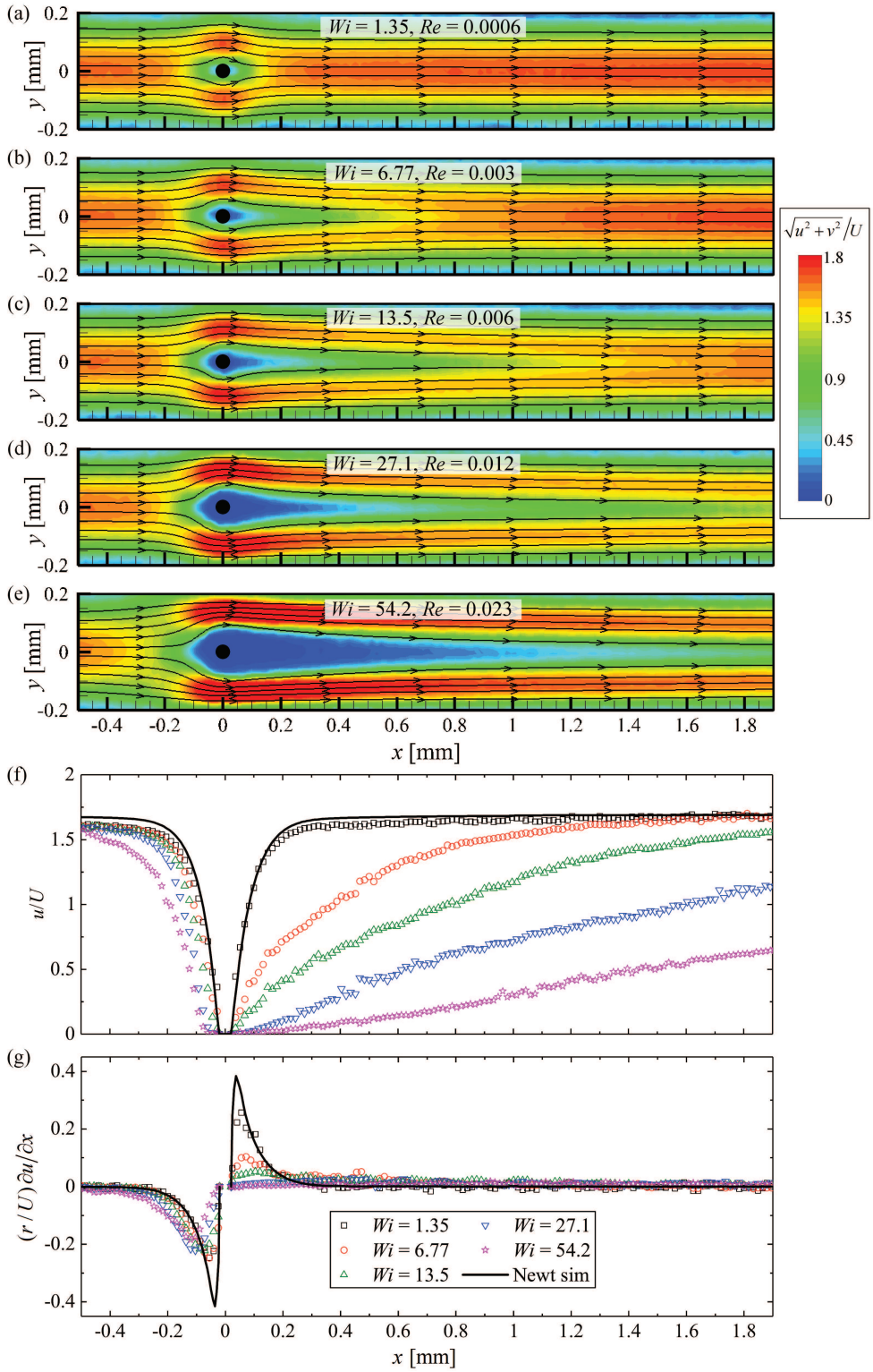

Figure 6: Flow field characterization around the cylinder in the sc device for a 0.07 wt% solution of PS7 in DOP. (a) to (e) Contours of the normalized velocity magnitude measured at the Weissenberg and Reynolds numbers indicated. (f) Normalized profiles of the streamwise flow velocity along the centre-line $u(x)/U$, and (g) normalized profiles of the streamwise velocity gradient $(r/U)\partial u/\partial x$ for various Weissenberg numbers. The solid lines in (f) and (g) represent the behaviour of a Newtonian fluid at $Re = 0.001$.

are: (1) increasingly significant modification of the flow field upstream of and laterally to the cylinder (as apparent from the increasingly large region of low velocity magnitude around the cylinder), and (2) increasing divergence of streamlines upstream of the cylinder around the region of low velocity magnitude.

By extracting velocity profiles from Figs. 6(a)-(e) along the $y = 0$ axis, the increasing degree of flow modification with Wi in the up- and downstream wake regions can be clearly quantified, see Fig. 6(f). The spatial derivative $\partial u/\partial x$ of the data in Fig. 6(f) gives the extensional rate along the flow axis. For each imposed Weissenberg number, this spatial derivative has been calculated numerically based on a central difference scheme and behaves as shown in Fig. 6(g). Upstream of the cylinder, there is a negative minimum in the extension rate due to the compressive flow leading to the upstream stagnation point. Downstream of the cylinder, there is a positive maximum in the extension rate due to the elongational flow leading away from the downstream stagnation point. In the Newtonian case (solid line), the upstream minimum and the downstream maximum rates are essentially equal and opposite. In the polymer solution, as Wi is increased, the modification of the flow field leads to a particularly severe reduction in the magnitude of the maximum extension rate measured downstream of the cylinder, which decays almost to zero. There is also a reduction in the magnitude of the upstream minimum rate, though significantly less severe. In Fig. 7(a) and Fig. 7(b) we show how the value of the downstream maximum and the upstream minimum in extension rate vary with the imposed Weissenberg number. Interestingly, when the velocity gradient is normalized using the polymer relaxation time λ (Fig. 7(b)) the maximum value in the downstream reaches a plateau of $\lambda\partial u/\partial x \approx 0.5$, as shown by the dotted black line. However, the minimum value measured upstream of the cylinder continues to scale approximately linearly with the imposed Weissenberg number, as shown by the dotted red line representing $\lambda\partial u/\partial x = -0.2Wi$. Fig. 7(c) provides the up- and downstream locations of the minima and maxima, respectively.

The flowtype parameter around the cylinder is also modi-

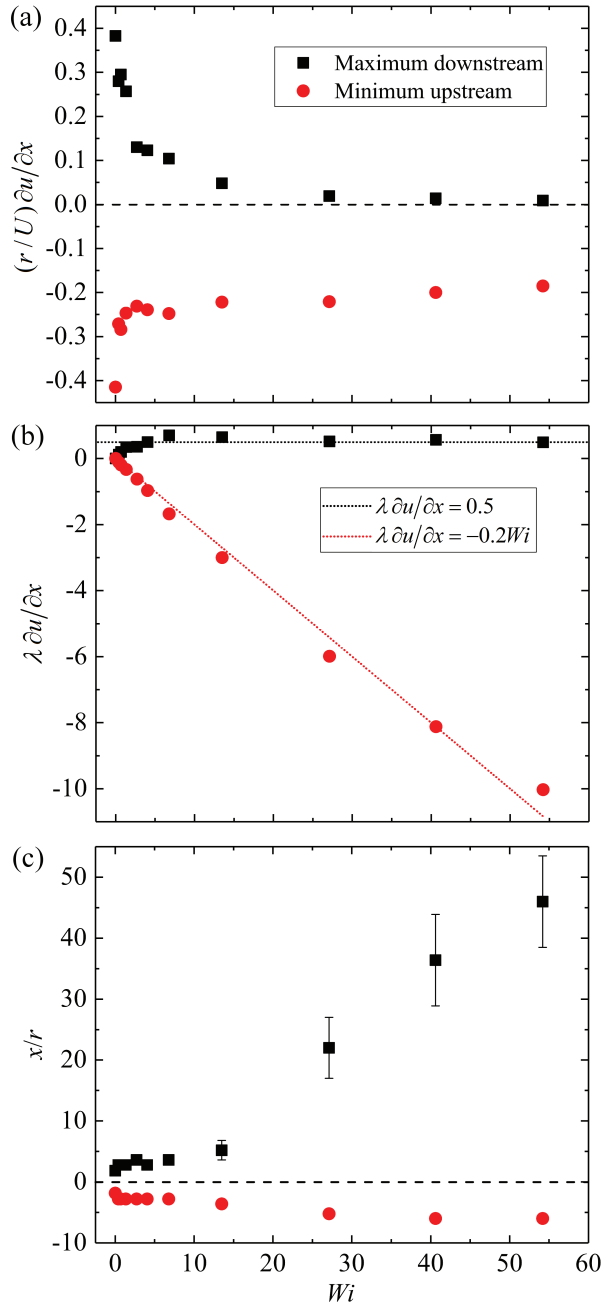

Figure 7: a) Value of the velocity gradient (non-dimensionalized by r/U) measured at the downstream maximum and the upstream minimum and (b) the same velocity gradient non-dimensionalized by λ. (c) Non-dimensionalized x-location of the downstream maximum and the upstream minimum velocity gradient as a function of the imposed Weissenberg number.

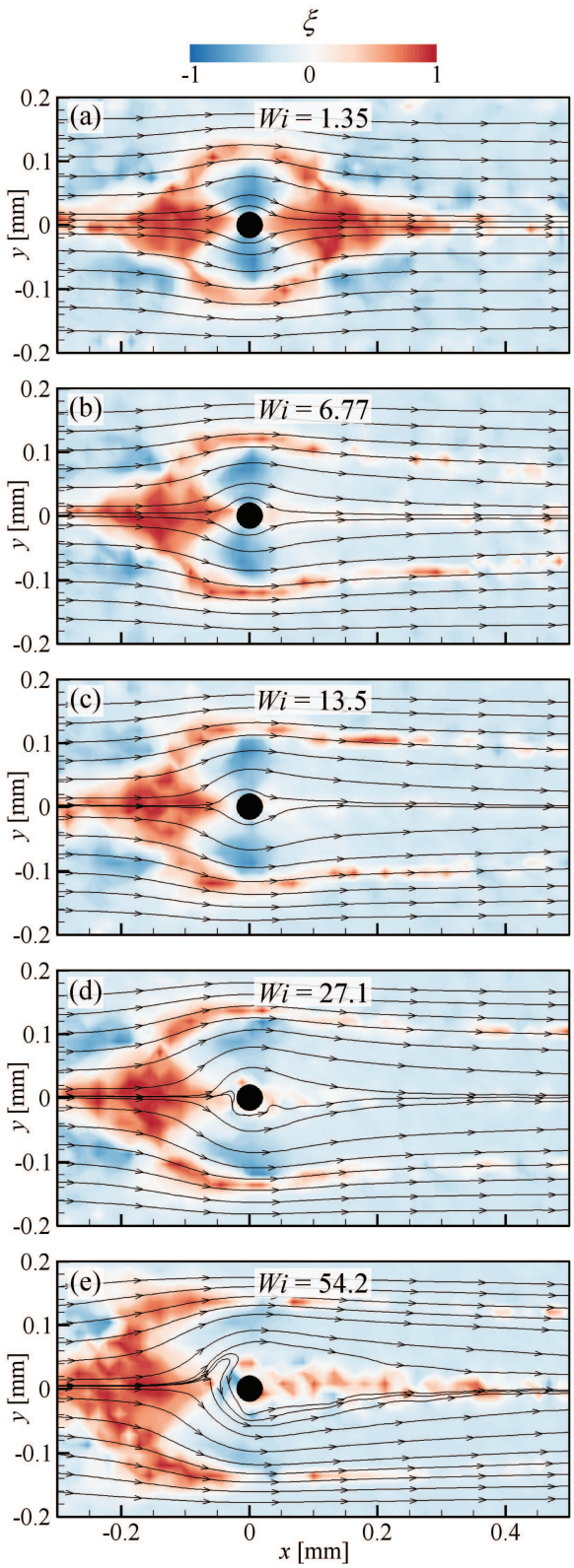

Figure 8: Flowtype parameter for polymeric flow around a cylinder as the Weissenberg number (indicated) is progressively increased through parts (a) to (e). Determined from μ-PIV measurements made in the sc device.

fied significantly as Wi is increased, as shown by Fig. 8. At lower Wi (Fig. 8(a)), the flowtype parameter is Newtonian-like, as expected (compare with Fig. 5). As Wi is increased, the extensional region upstream of the cylinder is maintained, but the extensional region in the downstream wake is all but lost and replaced by shear-dominated flow (Fig. 8(b,c)). At higher Wi the upstream region of extension dominated flow becomes enlarged and shifts upstream, with a small region of shear flow appearing at the leading surface of the cylinder (Fig. 8(d,e)). Here, in these slightly zoomed-in images, the emergence of a flow instability upstream of the cylinder is apparent. This is particularly clear in Fig. 8(e), with a significant distortion of the streamlines that select a preferential path around the bottom side of the cylinder. Similar upstream buckling of streamlines has been reported recently for flow of high molecular weight poly(acrylamide) solutions in a microfluidic cylinder device ($\alpha = 0.4$, $\beta = 0.2$) [25]. However, in that case the instability was time-dependent and fluctuating, while in the present case the instability remains steady (at least on the timescale and within the spatial resolution of the measurement).

Flow-induced birefringence measurements for flow of the polymer solution around the single cylinder are shown in Fig. 9. Clear FIB signals could only be measured for rather higher Weissenberg numbers $Wi \gtrsim 13.5$. The most striking feature of the images shown in Fig. 9 is the growth of the extremely elongated downstream wake as the Weissenberg number becomes large. At $Wi = 27.1$ the birefringence persists for some 3 mm ($150r$), while at $Wi = 54.2$ the birefringence persists for at least 6 mm ($300r$) into the downstream. Taking the average flow velocity at $Wi = 54.2$ ($U = 83.3$ mm s^{-1}) a flow time of $6/83.3 = 0.072$ seconds can be estimated, which is approximately 5 relaxation times of the polymer ($\lambda = 0.013$ s). However, given the severe reduction in the centerline flow velocity apparent from Figs. 6(e) and (f), the true transit time of fluid elements from the rear stagnation point to a location 6 mm downstream will be significantly greater than the estimate of 72 ms. By integrating over the flow velocimetry data provided in Fig. 6(f), it can be estimated that a fluid element would re-

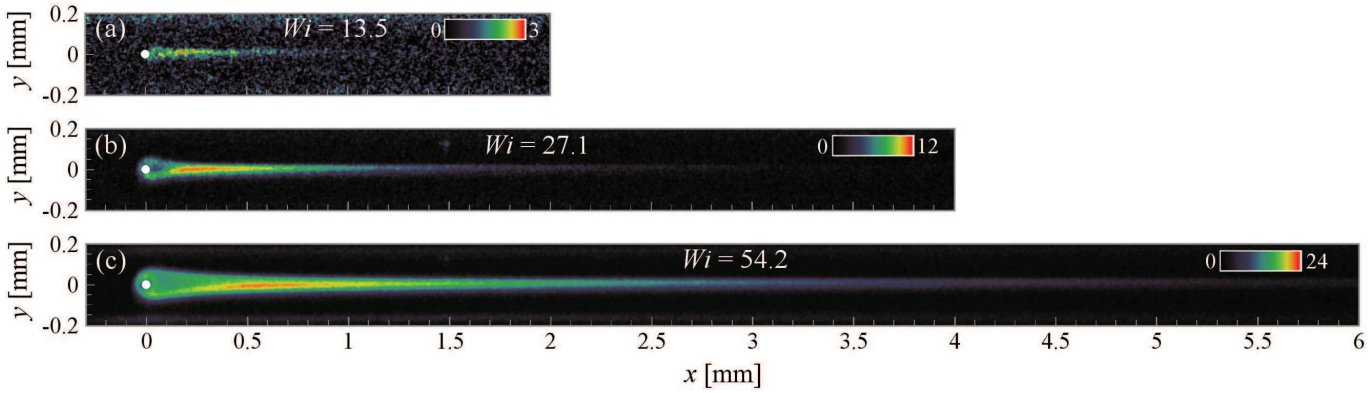

Figure 9: Flow-induced birefringence around and in the downstream wake of the single cylinder as the Weissenberg number (indicated) is progressively increased through parts (a) to (c). The colour scale bar indicates the retardance, R, in nanometers.

quire $\approx$ 0.38 s (i.e. $\approx 30\lambda$) for transport over the first 1.9 mm along the centreline downstream of the cylinder.

Apart from the striking downstream wake region, close inspection of the birefringence images in Fig. 9 reveals the presence of birefringence both upstream and around the sides of the cylinder (this is especially apparent in Fig. 9(c)). The regions where birefringence is measured correspond to regions where polymer molecules become oriented by the strong velocity gradients in the flow field, and the magnitude of the birefringence is indicative of the magnitude of the elastic tensile stress. The locations and magnitudes of the stress observed in Fig. 9 are clearly commensurate with the degree of flow modification observed in Fig. 6. On close inspection of Fig. 9(b,c) it can also be noticed that there is some lateral asymmetry of the birefringence in the downstream wake, with a strand of higher intensity birefringence appearing to originate from below the cylinder (i.e. from negative y). This is most likely explained by the upstream flow instability shown in Fig. 8(d,e), in which it is seen that streamlines become concentrated around the bottom side of the cylinder due to their selection of a preferential flow path.

Taken together, the results presented in Figs. 6-9 clearly indicate that the stretching of polymers in higher Wi flows is initiated in the extensional flow upstream of the cylinder, and not at the trailing stagnation point as generally supposed and predicted by models (e.g. Ref. [2]). The effect of the upstream stretching of the polymer, and the advection of the stretched molecules around the cylinder, effectively cloacks the cylinder in a jacket of highly stressed, locally viscosified fluid. This has the effect of making the cylinder radius appear to increase with the Weissenberg number. Hence, as Wi is increased, the leading edge of the cylinder is effectively shifted upstream, displacing the region of extensional flow upstream also, and streamlines diverge more significantly around the expanded circumference of the cylinder. The already stretched polymer molecules are subsequently advected around the cylinder into the downstream wake where they begin to relax. The downstream stagnation point is largely screened from the flow field by the strands of highly stressed fluid entering the downstream wake and the large extensional flow region downstream of the cylinder is lost (as shown in Fig. 8). There is some addition stretching of polymer close to the flow axis in the downstream wake, where a localized region of extensional flow remains (see Figs. 8 and 9). The subsequent slow relaxation of the polymer strain and elastic stress in the downstream is most likely explained by coil→stretch hysteresis [61–64], resulting in flow modifcation extending many cylinder radii (and many relaxation times) downstream. We note that ours are the first FIB measurements to be made for polymer solutions flowing around microfluidic cylinders, which is made possible here by the relatively large height, H, of our SLE-fabricated device. However, direct observations of polymer orientation in flow around a microscale cylinder were presented by François *et al* [11], by visualizing fluorescently-

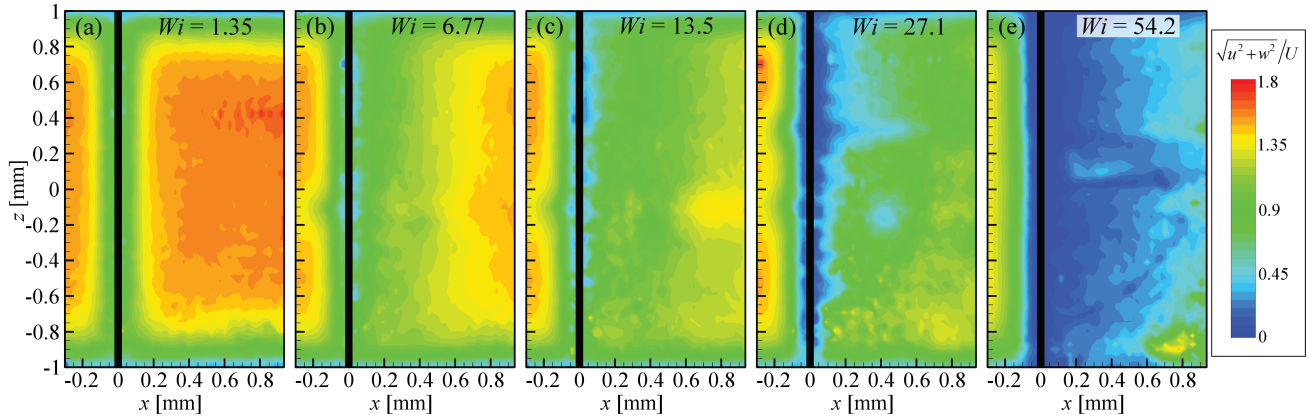

Figure 10: Contours of the normalized velocity magnitude measured in the xz plane at $y = 0$ as the Weissenberg number (indicated) is progressively increased through parts (a) to (e).

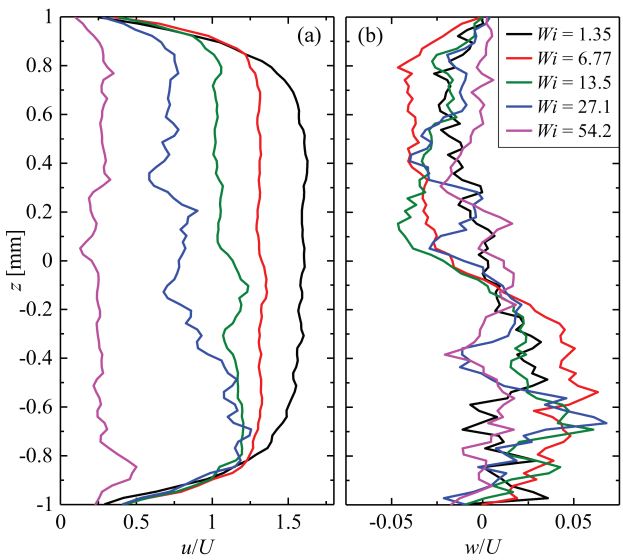

Figure 11: Normalized profiles of the flow velocity along the axial (z) direction taken 0.0768 mm (3.84r) downstream of the cylinder: (a) streamwise velocity component $u(z)/U$, (b) axial velocity component $w(z)/U$.

labelled long chain DNA tracer molecules contained in solutions of poly(ethylene oxide). Their data clearly show the strong stretching of the DNA molecules upstream of the cylinder and their advection in the already stretched state around the sides of the cylinder and into the downstream, supporting the assertions made here based on our own results. While François *et al* [11] did not examine the effects of the macromolecular deformation on the flow field around the cylinder, they showed that it resulted in a significant increase in the drag force on the cylinder. This would also be expected given the increasingly large polymeric stress that is evident as the Weissenberg number is increased in the birefringence images that we present in Fig. 9.

Previous authors using 'macroscopic' cylinder geometries with radii $r > 1$ mm have described the existence of an elastic wake instabilty resulting in the development of 3D cellular structure immediately downstream of a cylinder during steady viscoelastic flow at $Wi > 1$ [12, 13]. The spatially periodic structure is evident in variations of the axial and streamwise velocity components measured along the axis of the cylinder and has a wavelength that scales closely with the cylinder radius, r [12, 13]. Given the possibility to measure such velocity components in our SLE-fabricated devices, we decided to investigate the formation of any similar cellular structure in the downstream wake of our single microfluidic cylinder (sc) device. Fields of the normalized velocity magnitude ($\frac{\sqrt{(u^2+w^2)}}{U}$)

measured in the $y = 0$ plane bisecting the circumference of the cylinder are shown for a range of Wi in Fig. 10. The streamwise and axial velocity components u and w have been extracted from these fields along the z-direction at a distance of $\approx 4r$ downstream of the cylinder, and the results are shown in Fig. 11(a) and (b), respectively. We observe rather homogeneous flow (perhaps surprisingly so) through the height of our device over the range of Wi examined, see Fig. 10. There is some evidence of slight inhomogeneity in $u(z)$ at higher Weissenberg numbers, see Fig. 11(a). There is also evidence of slight axial velocity components ($w(z)$) directed away from the top and bottom channel walls (though only of around $0.05U$ at most), see Fig. 11(b). However, our measurements do not indicate the existence of any regular structure in the wake. It is important to mention here, that the μ-PIV results shown in Figs. 10 and 11 were obtained using a 5× NA= 0.15 objective lens, which is the highest magnification for which the entire height of the channel can be visualized. Using this lens, the measurement width through y is $\delta_m \approx 124$ μm [44] and vectors are obtained spaced at 12.8 μm intervals in x and z. Assuming the wavelength of the cellular structure continues to scale with the radius as the cylinder becomes very small, the spatial resolution of our velocity field measurements may not be sufficient to accurately resolve it. Furthermore the averaging of the velocity field over the significant measurement width $\delta_m \approx 6r$ would serve to mask any small periodic variations in the velocity immediately behind the cylinder axis. Therefore our attempts here to examine this cellular wake instability phenomenon for the first time in a microfluidic cylinder geometry have unfortunately proven inconclusive. We have performed additional measurements utilizing a 10× NA= 0.3 objective, for which the measurement width is $\delta_m \approx 39$ μm (i.e. $\approx 2r$) and the spatial resolution is also improved, however with this system we also did not observe any evidence of period structures in the wake (data not shown).

3.3. *Polymeric flow around two aligned cylinders*

In this section we examine polymeric flow in the dc channel, which contains two axially-aligned cylinders of radius $r = 20$ μm widely spaced by a centre-centre distance of $L = 1$ mm (i.e. $L = 50r$). The problem is relevant to understanding interactions that take place in viscoelastic flows around repeated sequences of objects such as settling particles, for which anomalous differences in drag between up- and downstream particles have been reported [9, 10, 65–67]. This experiment is also relevant to understanding flows of polymer solutions through periodic arrays of cylinders, which are frequently used as models for porous media flows [60, 68–73].

First, in Fig. 12, we examine how the flow field around the two aligned cylinders depends upon the imposed Weissenberg number. At fairly low $Wi = 1.35$ (Fig. 12(a)) the flow field appears Newtonian-like, as expected (compare with the result for purely Newtonian creeping flow shown in Fig. 4(b)). At sightly higher $Wi = 6.77$ (Fig. 12(b)), non-Newtonian flow modification effects become evident and each of the two cylinders develops an extended downstream wake. At this Wi, the wake behind cylinder 1 decays in the gap between the two cylinders and the flow field largely redevelops its parabolic profile before reaching cylinder 2. The wake around each cylinder is similar and also comparable with that observed around the cylinder in the sc device at the same Wi (see Fig. 6(b)). As Wi is increased further (Fig. 12(c-e)), the wake downstream of cylinder 1 reaches all the way across the gap as far as cylinder 2. Now, an increasing disparity between the wakes around cylinders 1 and 2 emerges with increasing Wi; flow modification around cylinder 2 appears to be significantly weaker than around cylinder 1.

We have attempted to understand and quantify these wake effects by examing the velocity profiles taken along the flow axis ($y = 0$), as shown for the dc geometry in Fig. 12(f). In this plot, it is visually obvious that for low $Wi = 1.35$ (black squares), the flow profile for the polymer solution closely matches the numerical prediction for creeping Newtonian flow ($Re = 0.001$, solid line). At $Wi = 6.77$ (red circles), the profiles behind cylinders 1 and 2 are both similar, however at higher Wi

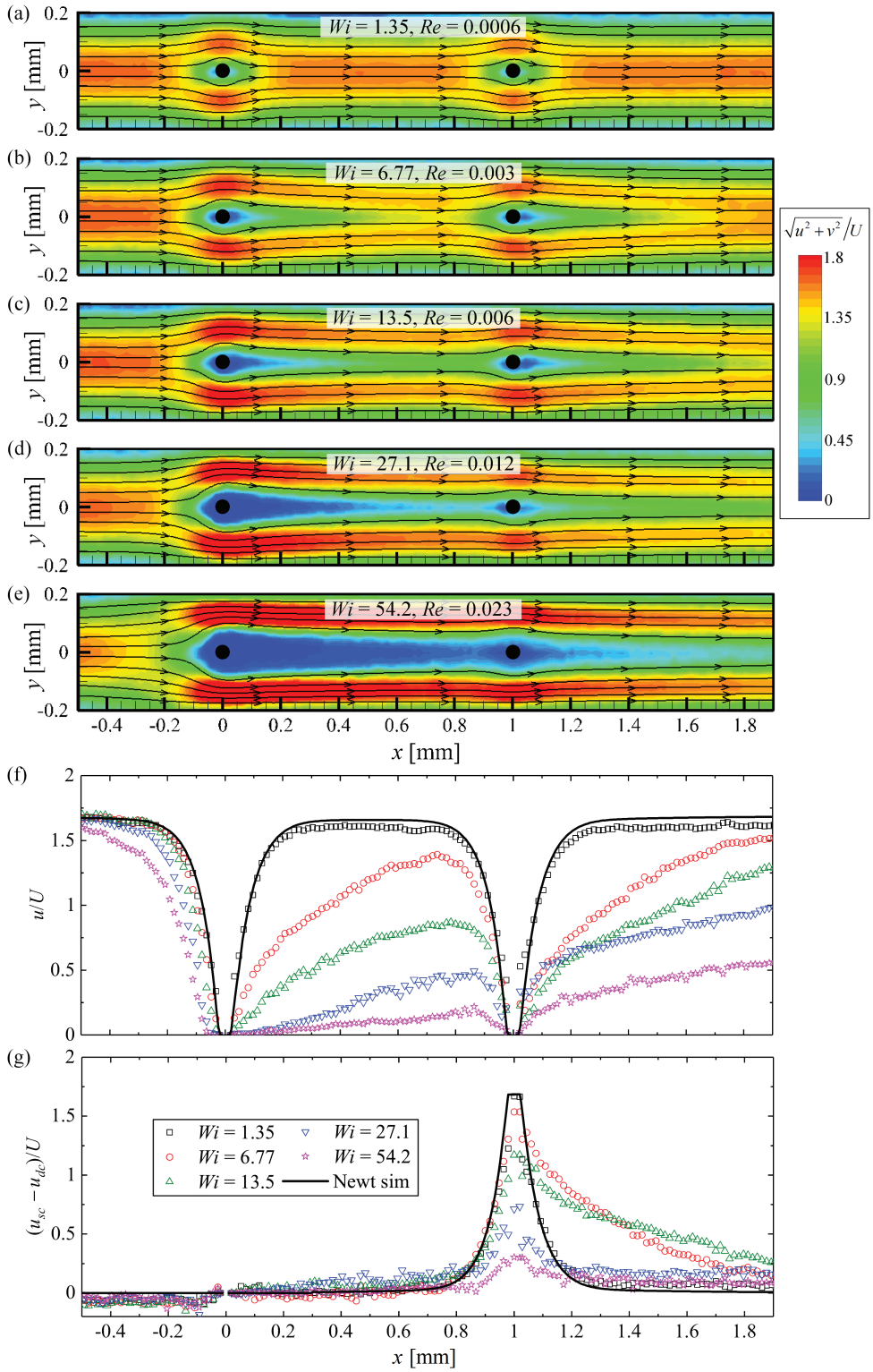

Figure 12: Flow field characterization around the cylinder in the dc device for a 0.07 wt% solution of PS7 in DOP. (a) to (e) Contours of the normalized velocity magnitude measured at the Weissenberg and Reynolds numbers indicated. (f) Normalized profiles of the streamwise flow velocity along the centre-line $u(x)/U$, and (g) a comparison between the flow profiles obtained in the sc and dc geometries under equivalent conditions. The solid lines in (f) and (g) represent the behaviour of a Newtonian fluid at $Re = 0.001$.

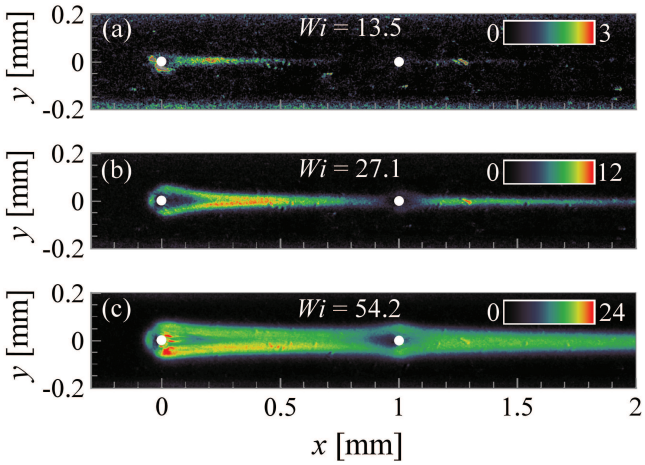

Figure 13: Flow-induced birefringence in the dc geometry as the Weissenberg number (indicated) is progressively increased through parts (a) to (c). The colour scale bar indicates the retardance, R, in nanometers.

the profiles behind each cylinder begin to differ. In fact for $Wi = 27.1$ (blue triangles) and $Wi = 54.2$ (magenta stars), the flow profile develops almost continuously from behind cylinder 1, with only a fairly minor dip at the location of cylinder 2.

The observations outlined above can be demonstrated more clearly by subtracting the wake profiles measured in the dc device from those measured in the sc device, as shown in Fig. 12(g). In the region upstream of cylinder 1, and in the gap between cylinders 1 and 2, this subtraction results in a collapse of the data close to zero, indicating that the wake around cylinder 1 in the dc device is very similar to the wake around a single cylinder (as might be expected). For the Newtonian fluid, there is a peak in the data at the location of cylinder 2, due to the reduction in the flow velocity around cylinder 2, which is absent in the sc geometry. The data for $Wi = 1.35$ closely follows the Newtonian curve, as expected. For $Wi = 6.77$ and $Wi = 13.5$, however, there is a clear extra wake behind cylinder 2 that is not present for Newtonian fluids and is also not present at these Weissenberg numbers in the sc device. Most interestingly, for $Wi = 27.1$ and $Wi = 54.2$ the subtraction behind cylinder 2 yields a value close to zero, showing that again the wake in the region behind cylinder 2 is similar to the wake behind a single cylinder. It appears as if (at these high Weissenberg numbers) cylinder 1 generates a wake similar to that of a single isolated cylinder, and that this wake relaxes continuously with distance downstream without being affected very much by the presence of the second cylinder.

Flow-induced birefringence measurements (shown in Fig. 13) lend support to the above discussion. At Weissenberg numbers $Wi \geq 13.5$ where birefringence can be detected, the signal in the downstream wake of cylinder 2 is significantly weaker than it is downstream of cylinder 1. Additionally, there is little or no birefringence evident immediately upstream of cylinder 2, as there is upstream of cylinder 1. The image obtained at $Wi = 54.2$ (Fig. 13(c)) shows most clearly that the highly stressed fluid originating from cylinder 1 is simply advected around cylinder 2 and continues to relax in the wake downstream of cylinder 2. Effectively, at higher Wi it appears as though cylinder 2 becomes encapsulated by the wake of cylinder 1 and ceases to play a significant role in the flow field.

Finally, in Fig. 14 we present the flowtype parameter around cylinder 2 of the dc geometry for a range of Wi. At low Wi (Fig. 14(a)), the flowtype parameter around cylinder 2 is quite similar to that around a single cylinder at the same Wi (Fig. 8(a)), which itself is similar to the flowtype measured around a single cylinder for creeping Newtonian flow (Fig. 5). As Wi is progressively increased (Fig. 14(b-e)), the extensional flow region downstream of cylinder 2 is lost (as it is in the downstream wake of a single cylinder, see (Fig. 8(b-e)). However, for cylinder 2, as Wi is increased there is also a signifcant and progressive diminishing of the upstream extensional flow region, which is not the case for flow around a single cylinder. At higher Wi (e.g. $Wi = 54.2$, Fig. 14(e)) the flow field around cylinder 2 is almost completely dominated by shear, with only very weak and localized extensional regions remaining. We also point out that at the higher Weissenberg numbers examined (Fig. 14(d,e)) streamlines diverge significantly less around cylinder 2 (Fig. 14(d,e)) than they do around the single cylinder (Fig. 8(d,e)). The buckling of streamlines reported upstream of the single cylinder (Fig. 8(d,e)) is also not observed upstream of cylinder 2. All of these observations confirm that as the wake of cylinder 1 begins to interact with cylinder 2, the role of cylin-

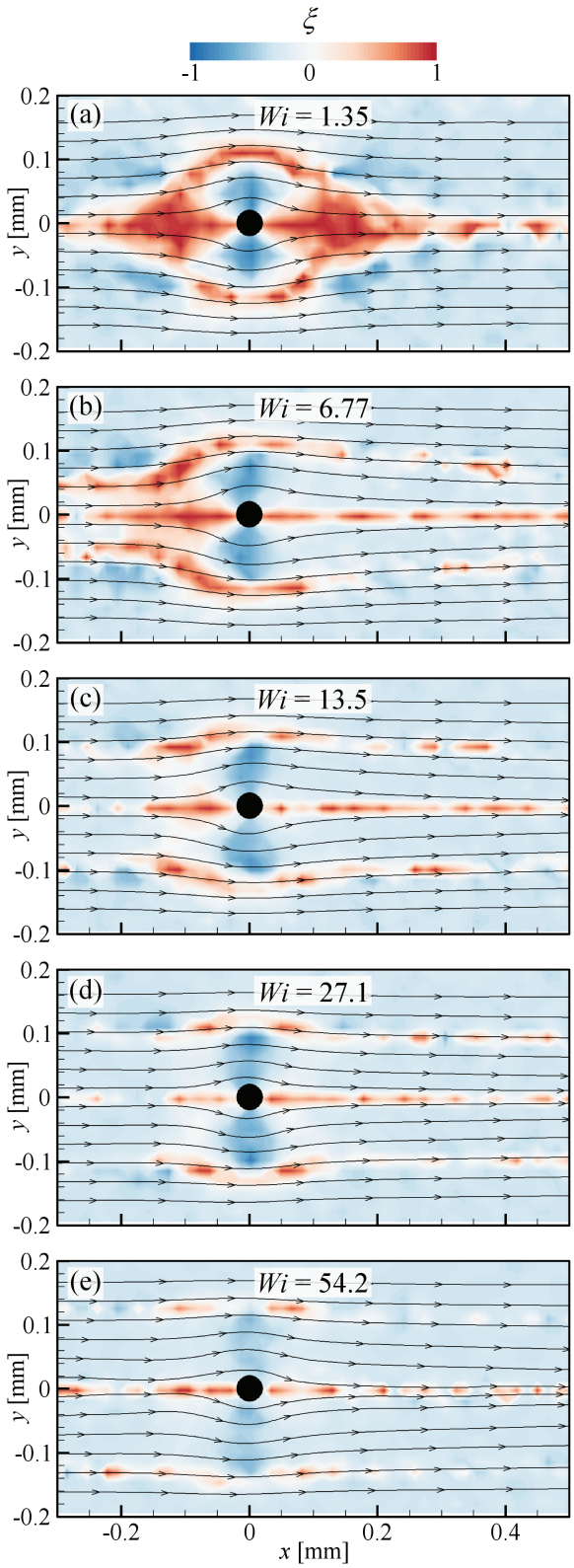

Figure 14: Flow type parameter around cylinder 2 in the dc device as the Weissenberg number (indicated) is progressively increased through parts (a) to (d).

der 2 in the flow field becomes of decreasing importance as the Weissenberg number is incremented further. In these high Wi flows, because cylinder 2 distorts the flow field very weakly compared with cylinder 1, and contributes much less to the generation of polymeric stress, it can be reasonably supposed that the non-Newtonian drag on cylinder 2 is also reduced compared with cylinder 1. This provides a possible explanation for some of the anomalous terminal velocity effects observed for the settling of spheres in viscoelastic fluids when falling along a common path [66, 67] and will also have relevance to understanding flows around e.g. clusters of cylindrical cilia and through porous media.

Conclusions

Using a state-of-the-art microfabrication technique, selective laser-induced etching, we have for the first time acheived the fabrication of microfluidic cylinder geometries that combine both high aspect ratios ($\alpha = 5$) and low blockage ratios ($\beta = 0.1$). Two devices have been produced, one containing a single cylinder of radius $r = 20\ \mu$m (sc device), and the second containing two axially cylinders ($r = 20\ \mu$m) separated by a distance of $50r$ (dc device). The devices are rigid, completely transparent and also resistant to organic solvents. Creeping flow of a viscous Newtonian fluid through the devices has been characterized using micro-particle image velocimetry (μ-PIV). The resulting flow profiles measured across the channel width and height show excellent agreement with the analytical prediction for Poiseuille flow in a rectangular channel of $\alpha = 5$. Flow profiles measured along the flow axis passing through the cylinders also compare well with finite volume numerical simulations performed at low Reynolds number. These controls confirm both the accuracy of our device fabrication method and also of our flow velocimetry technique.

Some intriguing behaviours are reported for the flow of a viscoelastic dilute solution of high molecular weight polystyrene through the cylinder geometries. Due to the small length scale r, the Reynolds numbers for the viscoelastic flow remain small $Re \lesssim 0.023$, while the Weissenberg numbers can be high $Wi \lesssim$

54, so that the flow occurs at high elasticity number $El = Wi/Re \approx 2400$. For flow in the sc device, as Wi is increased, we observe the growth of elastic stresses around the cylinder and in an extremely elongated downstream wake region ($> 300r$ in length), which is accompanied by strong modification of the velocity field compared with the Newtonian case. We consider that deformation of the polymer occurs principally in the extensional flow dominated region upstream of the cylinder. This highly stressed elastic fluid is advected around the sides of the cylinder and finally into the downstream wake where it commences to relax. The region of strong extensional flow normally present in the downstream wake of the cylinder becomes screened from the flow field and and is replaced by shear-dominated kinematics. As Wi is increased, the extensional rate dowstream of the cylinder becomes significantly and progressively reduced. However, upstream of the cylinder extensional kinematics remain present and the extensional rate remains high. An elastic flow asymmetry becomes apparent upstream of the cylinder as the Weissenberg number becomes high.

For viscoelastic flow around two aligned cylinders we find for low to moderate Wi the two cylinders are effectively in isolation from each other and have a similar impact on the flow field. However, for higher Weissenberg numbers the downstream wake of the first cylinder begins to interact with the second cylinder and consequently the two cylinders begin to show a strongly unequal response to the imposed flow. Our results indicate the upstream cylinder is dominant and that the downstream cylinder becomes effectively encapsulated in its extended downstream wake, playing only a minor role in the flow. Our results are expected to provide a useful comparison for benchmarking of viscoelastic constitutive models used in numerical simulations as well as being of fundamental interest and relevance to widespread applications.

Acknowledgements

We gratefully acknowledge the support of the Okinawa Institute of Science and Technology Graduate University (OIST) with subsidy funding from the Cabinet Office, Government of Japan. A.Q.S. also acknowledges funding from the Japan Society for the Promotion of Science (Grants-in-Aid for Scientific Research (C), Grant No. 17K06173). Mr San To Chan (OIST) is thanked for performing Newtonian flow simulations with ANSYS Fluent. Professor Robert J. Poole (University of Liverpool) is thanked for comments on the manuscript prior to submission.

References

[1] R. A. Brown, G. H. McKinley, Report on the VIIIth international workshop on numerical methods in viscoelastic flows, J. Non-Newtonian Fluid Mech. 52 (3) (1994) 407–413. doi:10.1016/0377-0257(94)85032-1.

[2] M. D. Chilcott, J. M. Rallison, Creeping flow of dilute polymer solutions past cylinders and spheres, J. Non-Newtonian Fluid Mech 29 (1-3) (1988) 381–432. doi:10.1016/0377-0257(88)85062-6.

[3] M. A. Alves, F. T. Pinho, P. J. Oliveira, The flow of viscoelastic fluid past a cylinder: Finite-volume high-resolution methods, J. Non-Newtonian Fluid Mech. 97 (2-3) (2001) 207–232. doi:10.1016/S0377-0257(00)00198-1.

[4] P. J. Oliveira, A. I. P. Miranda, A numerical study of steady and unsteady viscoelastic flow past bounded cylinders, J. Non-Newtonian Fluid Mech. 127 (1) (2005) 51–66. doi:10.1016/j.jnnfm.2005.02.003.

[5] V. M. Ribeiro, P. M. Coelho, F. T. Pinho, M. A. Alves, Viscoelastic fluid flow past a confined cylinder: Three-dimensional effects and stability, Chem. Eng. Sci. 111 (2014) 364–380. doi:10.1016/j.ces.2014.02.033.

[6] R. Cressely, R. Hocquart, Biréfringence d'écoulement localisée induite á l'arriére d'obstacles, Optica Acta 27 (1980) 699–711. doi:10.1080/713820288.

[7] M. J. Solomon, S. J. Muller, Flow past a sphere in polystyrene-based Boger fluids: The effect on the drag coefficient of finite extensibility, solvent quality and polymer molecular weight, J. Non-Newtonian Fluid Mech. 62 (1) (1996) 81–94. doi:10.1016/0377-0257(95)01398-9.

[8] D. Fabris, S. J. Muller, D. Liepmann, Wake measurements for flow around a sphere in a viscoelastic fluid, Phys. Fluids 11 (12) (1999) 3599–3612. doi:10.1063/1.870225.

[9] S. J. Haward, J. A. Odell, Molecular orientation in non-Newtonian flow of dilute polymer solutions around spheres, Rheol. Acta 43 (4) (2004) 350–363. doi:10.1007/s00397-003-0350-7.

[10] J. A. Odell, S. J. Haward, Viscosity enhancement in the flow of hydrolysed poly(acrylamide) saline solutions around spheres: Implications for enhanced oil recovery, Rheol. Acta 47 (2) (2008) 129–137. doi:10.1007/s00397-007-0220-9.

[11] N. François, D. Lasne, Y. Amarouchene, B. Lounis, H. Kellay, Drag

enhancement with polymers, Phys. Rev. Lett. 100 (1) (2008) 018302. doi:10.1103/PhysRevLett.100.018302.

[12] G. H. McKinley, R. C. Armstrong, R. A. Brown, The wake instability in viscoelastic flow past confined circular cylinders, Phil. Trans. R. Soc. Lond. A 344 (1671) (1993) 265–304. doi:10.1098/rsta.1993.0091.

[13] A. H. Shiang, A. Ötekin, J.-C. Lin, D. Rockwell, Hydroelastic instabilities in viscoelastic flow past a cylinder confined in a channel, Exp. Fluids 28 (2) (2000) 128–142. doi:10.1007/s003480050017.

[14] J. M. Verhelst, F. T. M. Nieuwstadt, Visco-elastic flow past circular cylinders mounted in a channel: experimental measurements of velocity and drag, J. Non-Newtonian Fluid Mech. 116 (2-3) (2004) 301–328. doi:10.1016/j.jnnfm.2003.08.006.

[15] C. J. Pipe, M. P. A., Vortex shedding in flows of dilute polymer solutions, J. Non-Newton. Fluid Mech. 139 (1-2) (2006) 54–67. doi:10.1016/j.jnnfm.2006.07.003.

[16] G. R. Moss, J. P. Rothstein, Flow of wormlike micelle solutions past a confined circular cylinder, J. Non-Newtonian Fluid Mech 165 (21-22) (2010) 1505–1515. doi:10.1016/j.jnnfm.2010.07.014.

[17] D. F. James, T. Shiau, P. M. Aldridge, Flow of a Boger fluid around an isolated cylinder, J. Rheol. 60 (6) (2016) 1137–1149. doi:10.1122/1.4961482.

[18] S. Kenney, K. Poper, G. Chapagain, G. F. Christopher, Large Deborah number flows around confined microfluidic cylinders, Rheol. Acta 52 (5) (2013) 485–497. doi:10.1007/s00397-013-0712-8.

[19] L. Pan, A. Morozov, C. Wagner, P. E. Arratia, Non-linear elastic instability in channel flows at low Reynolds number, Phys. Rev. Lett. 110 (17) (2013) 174502. doi:10.1103/PhysRevLett.110.174502.

[20] F. J. Galindo-Rosales, L. Campo-Deaño, P. C. Sousa, V. M. Ribeiro, M. S. N. Oliveira, M. A. Alves, F. T. Pinho, Viscoelastic instabilities in micro-scale flows, Exp. Them. Fluid Sci. 59 (2014) 128–139. doi:10.1016/j.expthermflusci.2014.03.004.

[21] X. Shi, S. Kenney, G. Chapagain, G. F. Christopher, Mechanisms of onset for moderate mach number instabilities of viscoelastic flows around confined cylinders, Rheol. Acta 54 (9-10) (2015) 805–815. doi:10.1007/s00397-015-0875-6.

[22] X. Shi, G. F. Christopher, Growth of viscoelastic instabilities around linear cylinder arrays, Phys. Fluids 28 (12) (2016) 124102. doi:10.1063/1.4968221.

[23] Y. Zhao, A. Q. Shen, S. J. Haward, Flow of wormlike micellar solutions around confined microfluidic cylinders, Soft Matter 12 (42) (2016) 8666–8681. doi:10.1039/c6sm01597b.

[24] C.-L. Sun, H.-Y. Huang, Measurements of flow-induced birefringence in microfluidics, Biomicrofluidics 10 (1) (2016) 011903. doi:10.1063/1.4939949.

[25] K. P. Nolan, A. Agarwal, S. Lei, R. Shields, Viscoelastic flow in an obstructed microchannel at high Weissenberg number, Microfluid. Nanofluid. 20 (7) (2016) 101. doi:10.1007/s10404-016-1765-7.

[26] A. Varshney, V. Steinberg, Elastic wake instabilities in a creeping flow between two obstacles, Phys. Rev. Fluids 2 (7) (2017) 05130. doi:10.1103/PhysRevFluids.2.051301.

[27] B. Qin, P. E. Arratia, Characterizing elastic turbulence in channel flows at low Reynolds number, Phys. Rev. Fluids 2 (8) (2017) 083302. doi:10.1103/PhysRevFluids.2.083302.

[28] C. Li, B. Qin, A. Gopinath, P. E. Arratia, B. Thomases, R. D. Guy, Flagellar swimming in viscoelastic fluids: Role of fluid elastic stress revealed by simulations based on experimental data, J. R. Soc. Interface 14 (135) (2017) 20170289. doi:10.1098/rsif.2017.0289.

[29] P. Pakdel, G. H. McKinley, Elastic instability and curved streamlines, Phys. Rev. Lett. 77 (12) (1996) 2459–2462. doi:10.1103/PhysRevLett.77.2459.

[30] G. H. McKinley, P. Pakdel, A. Öztekin, Rheological and geometric scaling of purely elastic flow instabilities, J. Non-Newtonian Fluid Mech. 67 (1996) 19–47. doi:10.1016/S0377-0257(96)01453-X.

[31] A. Öztekin, B. Alakus, G. H. McKinley, Stability of planar stagnation flow of a highly viscoelastic fluid, J. Non-Newtonian Fluid Mech. 72 (1) (1997) 1–29. doi:10.1016/S0377-0257(97)00021-9.

[32] S. J. Muller, Elastically-influenced instabilities in Taylor-Couette and other flows with curved streamlines: a review, Korea-Aust. Rheol. J. 20 (3) (2008) 117–125.

[33] P. E. Arratia, C. C. Thomas, J. Diorio, J. P. Gollub, Elastic instabilities of polymer solutions in cross-channel flow, Phys. Rev. Lett. 96 (14) (2006) 144502. doi:10.1103/PhysRevLett.96.144502.

[34] S. J. Haward, G. H. McKinley, A. Q. Shen, Elastic instabilities in planar elongational flow of monodisperse polymer solutions, Scientific Reports 6 (2016) 33029. doi:10.1038/srep33029.

[35] L. E. Rodd, T. P. Scott, D. V. Boger, J. J. Cooper-White, G. H. McKinley, The inertio-elastic planar entry flow of low-viscosity elastic fluids in micro-fabricated geometries, J. Non-Newtonian Fluid Mech. 129 (1) (2005) 1–22. doi:10.1016/j.jnnfm.2005.04.006.

[36] L. E. Rodd, J. J. Cooper-White, D. V. Boger, G. H. McKinley, Role of the elasticity number in the entry flow of dilute polymer solutions in micro-fabricated contraction geometries, J. Non-Newtonian Fluid Mech 143 (2-3) (2007) 170–191. doi:10.1016/j.jnnfm.2007.02.006.

[37] T. J. Ober, S. J. Haward, C. J. Pipe, J. Soulages, G. H. McKinley, Microfluidic extensional rheometry using a hyperbolic contraction geometry, Rheol. Acta 52 (6) (2013) 529–46. doi:10.1007/s00397-013-0701-y.

[38] J. Gottmann, M. Hermans, J. Ortmann, Digital photonic production of micro structures in glass by in-volume selective laser-induced etching using a high speed micro scanner, Physics Procedia 39 (2012) 534–541. doi:10.1016/j.phpro.2012.10.070.

[39] G. Meineke, M. Hermans, J. Klos, A. Lenenbach, R. Noll, A microfluidic opto-caloric switch for sorting of particles by using 3D-hydrodynamic focusing based on SLE fabrication capabilities, Lab Chip 16 (5) (2016) 820–828. doi:10.1039/C5LC01478F.

[40] W. W. Graessley, Polymer chain dimensions and the dependence of

viscoelastic properties on concentration, molecular weight and solvent power, Polymer 21 (3) (1980) 258–262. doi:10.1016/0032-3861(80)90266-9.

[41] S. J. Haward, M. S. N. Oliveira, M. A. Alves, G. H. McKinley, Optimized cross-slot geometry for microfluidic extensional rheometry, Phys. Rev. Lett. 109 (12) (2012) 128301. doi:10.1103/PhysRevLett.109.128301.

[42] B. H. Zimm, Dynamics of polymer molecules in dilute solution: Viscoelasticity, flow birefringence and dielectric loss, J. Chem. Phys. 24 (2) (1956) 269–278. doi:10.1063/1.1742462.

[43] F. Del Giudice, S. J. Haward, A. Q. Shen, Relaxation time of dilute polymer solutions: A microfluidic approach, J. Rheol. 61 (2) (2017) 327–337. doi:10.1122/1.4975933.

[44] C. D. Meinhart, S. T. Wereley, M. H. B. Gray, Volume illumination for two-dimensional particle image velocimetry, Meas. Sci. Technol. 11 (6) (2000) 809–814. doi:10.1088/0957-0233/11/6/326.

[45] C.-Y. Han, Y.-F. Chao, Photoelastic modulated imaging ellipsometry by stroboscopic illumination technique, Rev. Sci. Instrum. 77 (2) (2006) 023107. doi:10.1063/1.2173027.

[46] S. Nichols, J. Freudenthal, O. Arteaga, B. Kahr, Imaging with photoelastic modulators, in: D. B. Chenault, D. H. Goldstein (Eds.), Polarization: Measurement, Analysis, and Remote Sensing XI, Vol. 9099, SPIE-Intl Soc Optical Eng, 2014, p. 909912. doi:10.1117/12.2053459.

[47] T. T. Perkins, D. E. Smith, S. Chu, Single polymer dynamics in an elongational flow, Science 276 (5321) (1997) 2016–2021. doi:10.1126/science.276.5321.2016.

[48] D. E. Smith, S. Chu, Response of flexible polymers to a sudden elongation flow, Science 281 (5381) (1998) 1335–1340. doi:10.1126/science.281.5381.1335.

[49] S. J. Haward, V. Sharma, J. A. Odell, Extensional opto-rheometry with biofluids and ultra-dilute polymer solutions, Soft Matter 7 (21) (2011) 9908–9921. doi:10.1039/c1sm05493g.

[50] G. G. Fuller, Optical Rheometry of Complex Fluids, Oxford University Press, New York, 1995.

[51] G. G. Fuller, L. G. Leal, Flow birefringence of dilute polymer solutions in two-dimensional flows, Rheol. Acta 19 (5) (1980) 580–600. doi:10.1007/BF01517512.

[52] J. M. Li, W. R. Burghardt, B. Yang, B. Khomami, Birefringence and computational studies of a polystyrene Boger fluid in axisymmetric stagnation flow, J. Non-Newtonian Fluid Mech. 91 (2-3) (2000) 189–220. doi:10.1016/S0377-0257(99)00094-4.

[53] J. P. Rothstein, G. H. McKinley, A comparison of the stress and birefringence growth of dilute, semi-dilute and concentrated polymer solutions in uniaxial extensional flows, J. Non-Newtonian Fluid Mech 108 (1-3) (2002) 275–290. doi:10.1016/S0377-0257(02)00134-9.

[54] V. Sharma, S. J. Haward, J. Serdy, B. Keshavarz, A. Soderlund, P. Threlfall-Holmes, G. H. McKinley, The rheology of aqueous solutions of ethyl hydroxy-ethyl cellulose (EHEC) and its hydrophobically modified analogue (hmEHEC): Extensional flow response in capillary break-up, jetting (ROJER) and in a cross-slot extensional rheometer, Soft Matter 11 (16) (2015) 3251–3270. doi:10.1039/c4sm01661k.

[55] D. C. Venerus, S. H. Zhu, H.-C. Öttinger, Stress and birefringence measurements during the uniaxial elongation of polystyrene melts, J. Rheol. 43 (3) (1999) 795–813. doi:10.1122/1.551004.

[56] R. K. Shah, A. L. London, Laminar flow forced convection in ducts:A source book for compact heat exchanger analytical data, Academic Press, New York, 1978.

[57] G. Astarita, Objective and generally applicable criteria for flow classification, J. Non-Newtonian Fluid Mech. 6 (1) (1979) 69–76. doi:10.1016/0377-0257(79)87004-4.

[58] M. S. N. Oliveira, F. T. Pinho, R. J. Poole, P. J. Oliveira, M. A. Alves, Purely elastic flow asymmetries in flow-focusing devices, J. Non-Newtonian Fluid Mech 160 (1) (2009) 31–39. doi:10.1016/j.jnnfm.2009.02.010.

[59] C. E. Wagner, G. H. McKinley, The importance of flow history in mixed shear and extensional flows, J. Non-Newtonian Fluid Mech. 233 (2016) 133–145. doi:10.1016/j.jnnfm.2016.02.007.

[60] E. J. Hemingway, A. Clarke, J. R. A. Pearson, S. M. Fielding, Thickening of viscoelastic flow in a model porous medium, J. Non-Newtonian Fluid Mech. 251 (2018) 56–68. doi:10.1016/j.jnnfm.2017.11.002.

[61] P. G. De Gennes, Coil-stretch transition of dilute flexible polymers under ultrahigh velocity gradients, J. Chem. Phys. 60 (12) (1974) 5030–5042. doi:10.1063/1.1681018.

[62] E. J. Hinch, Mechanical models of dilute polymer solutions in strong flows, Phys. Fluids 20 (10) (1977) S22–S30. doi:10.1063/1.861735.

[63] C. M. Schroeder, H. P. Babcock, E. S. G. Shaqfeh, S. Chu, Observation of polymer conformation hysteresis in extensional flow, Science 301 (5639) (2003) 1515–1519. doi:10.1126/science.1086070.

[64] S. J. Haward, J. A. Odell, Z. Li, X.-F. Yuan, Extensional rheology of dilute polymer solutions in oscillatory cross-slot flow: The transient behavior of birefringent strands, Rheol. Acta 49 (6) (2010) 633–645. doi:10.1007/s00397-009-0420-6.

[65] M. J. Riddle, C. Narvaez, R. B. Bird, Interactions between two spheres falling along their line of centres in a viscoelastic fluid, J. Non Newtonian Fluid Mech. 2 (1) (1977) 23–35. doi:10.1016/0377-0257(77)80030-X.

[66] C. Bisgaard, Velocity fields around spheres and bubbles investigated by laser-doppler velocimetry, J. Non-Newtonian Fluid Mech. 12 (3) (1983) 283–302. doi:10.1016/0377-0257(83)85003-4.

[67] W. M. Jones, A. H. Price, K. Walters, The motion of a sphere falling under gravity in a constant-viscosity elastic liquid, J. Non-Newtonian Fluid Mech. 53 (1994) 175–196. doi:10.1016/0377-0257(94)85048-8.

[68] L. Campo-Deaño, F. J. Galindo-Rosales, F. T. Pinho, M. A. Alves, M. S. N. Oliveira, Nanogel formation of polymer solutions flowing through porous media, Soft Matter 8 (24) (2012) 6445–6453. doi:10.1039/c2sm25654a.

[69] D. F. James, R. Yip, I. G. Currie, Slow flow of boger fluids through model fibrous porous media, J. Rheol. 56 (5) (2012) 1249–1277. doi:10.1122/1.4732533.

[70] D. F. James, N_1 stresses in extensional flows, J. Non-Newtonian Fluid Mech. 232 (2016) 33–42. doi:10.1016/j.jnnfm.2016.01.012.

[71] S. De, J. van der Schaaf, N. G. Deen, J. A. M. Kuipers, E. A. J. F. Peters, J. T. Padding, Lane change in flows through pillared microchannels, Phys. Fluids 29 (11) (2017) 113102. doi:10.1063/1,4995371.

[72] D. Kawale, E. Marques, P. L. J. Zitha, M. T. Kreutzer, W. R. Rossen, P. E. Boukany, Elastic instabilities during the flow of hydrolyzed polyacrylamide solution in porous media: Effect of pore-shape and salt, Soft Matter 13 (4) (2017) 765–775. doi:10.1039/c6sm02199a.

[73] D. Kawale, G. Bouwman, S. Sachdev, P. L. J. Zitha, M. T. Kreutzer, W. R. Rossen, P. E. Boukany, Polymer conformation during flow in porous media, Soft Matter 13 (46) (2017) 8745–8755. doi:10.1039/c7sm00817a.